



Unbiased discovery of autoantibodies associated with severe COVID-19 via genome-scale self-assembled DNA-barcoded protein libraries

Joel J. Credle^{1,17}, Jonathan Gunn^{1,17}, Puwanat Sangkhaapreecha¹, Daniel R. Monaco¹, Xuwen Alice Zheng¹, Hung-Ji Tsai², Azaan Wilbon¹, William R. Morgenlander¹, Andre Rastegar¹, Yi Dong³, Sahana Jayaraman¹, Lorenzo Tosi⁴, Biju Parekkadan⁴, Alan N. Baer⁵, Mario Roederer⁶, Evan M. Bloch⁷, Aaron A. R. Tobian⁷, Israel Zyskind^{8,9}, Jonathan I. Silverberg¹⁰, Avi Z. Rosenberg¹¹, Andrea L. Cox¹², Tom Lloyd^{13,14}, Andrew L. Mammen^{13,15,16} and H. Benjamin Larman¹  

Pathogenic autoreactive antibodies that may be associated with life-threatening coronavirus disease 2019 (COVID-19) remain to be identified. Here, we show that self-assembled genome-scale libraries of full-length proteins covalently coupled to unique DNA barcodes for analysis by sequencing can be used for the unbiased identification of autoreactive antibodies in plasma samples. By screening 11,076 DNA-barcoded proteins expressed from a sequence-verified human ORFeome library, the method, which we named MIPSAs (for Molecular Indexing of Proteins by Self-Assembly), allowed us to detect circulating neutralizing type-I and type-III interferon (IFN) autoantibodies in five plasma samples from 55 patients with life-threatening COVID-19. In addition to identifying neutralizing type-I IFN- α and IFN- ω autoantibodies and other previously known autoreactive antibodies in patient plasma, MIPSAs enabled the detection of as yet unidentified neutralizing type-III anti-IFN- λ 3 autoantibodies that were not seen in healthy plasma samples or in convalescent plasma from ten non-hospitalized individuals with COVID-19. The low cost and simple workflow of MIPSAs will facilitate unbiased high-throughput analyses of protein-antibody, protein-protein and protein-small-molecule interactions.

An unbiased analysis of antibody-binding specificities can provide insights into states of health and disease. We and others have used programmable phage-display libraries to identify novel autoantibodies, to characterize antiviral immunity and to profile allergen-specific IgE antibodies^{1–5}. Although phage display has been useful for these and many other applications, most protein–protein, protein–antibody and protein–small-molecule interactions require a degree of conformational structure that is not captured by bacteriophage-displayed peptide libraries. Profiling conformational protein interactions at proteome scale has traditionally relied on protein microarray technologies. Protein microarrays, however, tend to suffer from high per-assay cost, and from a myriad of technical artefacts, including those associated with the high-throughput expression and purification of proteins, the spotting of proteins onto a solid support, the drying and rehydration of arrayed proteins and the readout of slides imaged via scanning fluorescence imaging^{6,7}.

Alternative approaches to protein-microarray production and storage have been developed (such as nucleic acid-programmable protein array, NAPPA⁸, or single-molecule polymerase chain reaction (PCR)-linked in vitro expression, SIMPLEX⁹). However, a robust, scalable and cost-effective alternative is lacking.

To overcome the limitations associated with the array-based profiling of full-length proteins, we previously established a methodology, which we named Parallel Analysis of Translated Open reading frames (PLATO), that uses ribosome display of open reading frame (ORF) libraries¹⁰. Ribosome display relies on the in vitro translation of messenger RNAs that lack stop codons, stalling ribosomes at the ends of mRNA molecules in a complex with the nascent proteins that they encode. PLATO suffers from several key limitations that have hindered its adoption. An ideal alternative is the covalent conjugation of proteins to short amplifiable DNA barcodes. Indeed, individually prepared DNA-barcoded antibodies and proteins have been

¹Institute for Cell Engineering, Division of Immunology, Department of Pathology, Johns Hopkins University School of Medicine, Baltimore, MD, USA.

²Institute of Microbiology and Infection, School of Biosciences, University of Birmingham, Edgbaston, Birmingham, UK. ³Center for Cell Dynamics and Department of Cell Biology, Johns Hopkins University School of Medicine, Baltimore, MD, USA. ⁴Department of Biomedical Engineering, Rutgers University, Piscataway, NJ, USA. ⁵Division of Rheumatology, Department of Medicine, Johns Hopkins University School of Medicine, Baltimore, MD, USA.

⁶ImmunoTechnology Section, Vaccine Research Center, NIAID, NIH, Bethesda, MD, USA. ⁷Division of Transfusion Medicine, Department of Pathology, Johns Hopkins University School of Medicine, Baltimore, MD, USA. ⁸Department of Pediatrics, NYU Langone Medical Center, New York City, NY, USA.

⁹Department of Pediatrics, Maimonides Medical Center, Brooklyn, NY, USA. ¹⁰Department of Dermatology, George Washington University School of Medicine and Health Sciences, Washington, DC, USA. ¹¹Division of Kidney-Urologic Pathology, Department of Pathology, Johns Hopkins University School of Medicine, Baltimore, MD, USA. ¹²Division of Infectious Diseases, Department of Medicine, Johns Hopkins University School of Medicine, Baltimore, MD, USA. ¹³Department of Neurology and Neurosurgery, Johns Hopkins University School of Medicine, Baltimore, MD, USA. ¹⁴Solomon H. Snyder Department of Neuroscience, Johns Hopkins University School of Medicine, Baltimore, MD, USA. ¹⁵Muscle Disease Unit, National Institute of Arthritis and Musculoskeletal and Skin Diseases, NIH, Bethesda, MD, USA. ¹⁶Department of Medicine, Johns Hopkins University School of Medicine, Baltimore, MD, USA. ¹⁷These authors contributed equally: Joel J. Credle, Jonathan Gunn. ✉e-mail: hlarman1@jhmi.edu

employed successfully in a variety of applications¹¹. One particularly attractive protein–DNA-conjugation method involves the HaloTag system, which adapts a bacterial enzyme that forms an irreversible covalent bond with halogen-terminated alkane moieties¹². Individual DNA-barcoded HaloTag fusion proteins have been shown to greatly enhance the sensitivity and dynamic range of autoantibody detection, compared with traditional enzyme-linked immunosorbent assay¹³. Scaling individual protein barcoding to entire ORFome libraries would be immensely valuable yet formidable, owing to high costs and low throughput. A self-assembly approach could provide a much more efficient path to library production.

In this Article, we describe a molecular-display technology, which we named Molecular Indexing of Proteins by Self-Assembly (MIPSA), that overcomes key disadvantages of PLATO and other full-length protein-array technologies. MIPSA produces libraries of soluble full-length proteins, each uniquely identifiable via covalent conjugation to an amplifiable DNA barcode. Barcodes are introduced upstream of the ribosome-binding site (RBS). Partial reverse transcription (RT) of the *in vitro* transcribed RNA (IVT-RNA) creates a complementary DNA barcode, which is linked to a haloalkane-labelled RT primer. An N-terminal HaloTag fusion protein is encoded downstream of the RBS, such that *in vitro* translation results in the intra-complex (*cis*) covalent coupling of the cDNA barcode to the HaloTag and its downstream ORF-encoded protein product. The resulting library of uniquely indexed full-length proteins can be used for inexpensive proteome-wide interaction studies, such as unbiased autoantibody profiling.

Coronavirus disease 2019 (COVID-19), caused by severe acute respiratory syndrome coronavirus 2 (SARS-CoV-2) infection, ranges from an asymptomatic course to life-threatening pneumonia and death. A causal link between autoimmunity and severe COVID-19 has been supported by multiple studies^{14,15}. Although a diverse array of autoantibodies have been documented¹⁶, neutralizing type-I interferon (IFN) autoantibodies seem to play a particularly prominent role^{17,18}. Here, we investigate the utility of MIPSA by searching for novel autoantibodies in the plasma of patients with severe COVID-19.

Results

Development of the MIPSA system. The MIPSA Gateway Destination vector for *Escherichia coli* cell-free translation contains the following key elements: a T7 RNA polymerase transcriptional start site, an isothermal unique clonal identifier (UCI) barcode sequence, an *E. coli* RBS, an N-terminal HaloTag fusion protein (891 nt), recombination sequences for ORF insertion and a homing endonuclease (I-SceI) site for plasmid linearization. A recombinant ORF-containing pDEST–MIPSA plasmid is shown in Fig. 1a.

We first sought to establish a library of pDEST–MIPSA plasmids containing stochastic, isothermal UCIs located between the transcriptional start site and the RBS. A degenerate oligonucleotide pool was synthesized, comprising melting temperature (T_m) balanced sequences: (SW)₁₈–AGGGA–(SW)₁₈, where S represents an equal mix of C and G, while W represents an equal mix of A and T (Fig. 1b). We reasoned that this inexpensive pool of sequences would (1) provide sufficient complexity ($2^{36} \sim 7 \times 10^{10}$) for unique ORF labelling, (2) amplify without distortion and (3) serve as ORF-specific forward and reverse quantitative PCR (qPCR) primer binding sites for measurement of individual UCIs of interest. The degenerate oligonucleotide pool was amplified by PCR, restriction cloned into the MIPSA destination vector and transformed into *E. coli* (Methods). About 800,000 transformants were scraped off selection plates to obtain the pDEST–MIPSA UCI plasmid library. ORFs encoding the housekeeping protein glyceraldehyde-3-phosphate dehydrogenase (GAPDH) and a known autoantigen, tripartite motif containing-21 (TRIM21, commonly known as Ro52) were separately recombined into the pDEST–MIPSA UCI plasmid library. Individually barcoded

GAPDH and *TRIM21* clones were isolated, sequenced and used in the following experiments.

The MIPSA procedure involves RT of the UCI using a succinimidyl ester (O₂)-haloalkane (HaloLigand)-conjugated RT primer (Supplementary Fig. 1). The bound RT primer should not interfere with the assembly of the *E. coli* ribosome and initiation of translation but should be sufficiently proximal such that coupling of the HaloLigand–HaloTag–protein complex might hinder additional rounds of translation (Fig. 1b,c). We tested a series of RT primers that anneal at distances ranging from –42 nucleotides to –7 nucleotides relative to the 5′ end of the RBS (Fig. 1d). On the basis of the yield of protein product from mRNA saturated with primers at these differing locations, we selected the –32 position as it did not interfere with translation efficiency (Fig. 1e). In contrast, RT from primers located within 20 nucleotides of the RBS diminished or abolished protein translation, in agreement with the estimated footprint of assembled 70S *E. coli* ribosomes, which have been shown to protect an average of 24 nucleotides of mRNA, with a range of 15 to 40 nucleotides.¹⁹

We next assessed the ability of SuperScript IV to perform RT from a primer labelled with the HaloLigand at its 5′ end, and the ability of the HaloTag–TRIM21 protein to form a covalent bond with the HaloLigand-conjugated primer during the translation reaction. HaloLigand conjugation and purification followed previously established methods. (Methods and Supplementary Fig. 1)²⁰. Either an unconjugated RT primer or a HaloLigand-conjugated RT primer was used for RT of the barcoded HaloTag–TRIM21 mRNA. The translation product was then immunocaptured (immunoprecipitated) with plasma from a healthy donor or plasma from a TRIM21 autoantibody-positive patient with Sjögren's syndrome (SS), using protein-A- and protein-G-coated magnetic beads. The SS plasma efficiently immunoprecipitated the TRIM21 protein, regardless of RT primer conjugation, but only pulled down the TRIM21 UCI when the HaloLigand-conjugated primer was used in the RT reaction (Fig. 1f,g).

Assessing levels of *cis* versus *trans* UCI barcoding. While the previous experiment indicated that, indeed, the HaloLigand does not impede RT priming and that the HaloTag can form a covalent bond with the HaloLigand during the translation reaction, it did not elucidate the amount of *cis* (intra-complex, desirable) versus *trans* (inter-complex, undesirable) HaloTag–UCI conjugation (Supplementary Fig. 2). Here, ‘intra-complex’ is defined as conjugation to the UCI that is associated with the same RNA molecule encoding the protein. To measure the amount of *cis* and *trans* HaloTag–UCI conjugation, *GAPDH* and *TRIM21* mRNAs were separately reverse transcribed (using HaloLigand-conjugated primer) and then either mixed 1:1 or kept separate for *in vitro* translation. As expected, translation of the mixture produced roughly equivalent amounts of each protein compared with the individual translations (Supplementary Fig. 3). SS plasma specifically immunoprecipitated TRIM21 protein regardless of translation condition (Supplementary Fig. 3, immunoprecipitated fraction). However, we noted that while the SS IPs contained high levels of the TRIM21 UCI, as intended, more of the GAPDH UCI was pulled down by the SS plasma compared with that by the healthy control (HC) plasma when the mRNA was mixed before translation. This indicates that indeed some amount of *trans* barcoding occurs (Fig. 2a). We estimate that ~50% of the protein is *cis*-barcoded, with the remaining 50% *trans*-barcoded protein equally conjugated to both UCIs. Thus, in this two-component system, 25% of the TRIM21 protein is conjugated to the GAPDH UCI (Supplementary Fig. 2).

In the setting of a complex library, even if ~50% of each protein is *trans* barcoded, this side product should be associated with a low level of randomly sampled UCIs. We tested this using a mock MIPSA library, composed of 100-fold excess of a second GAPDH

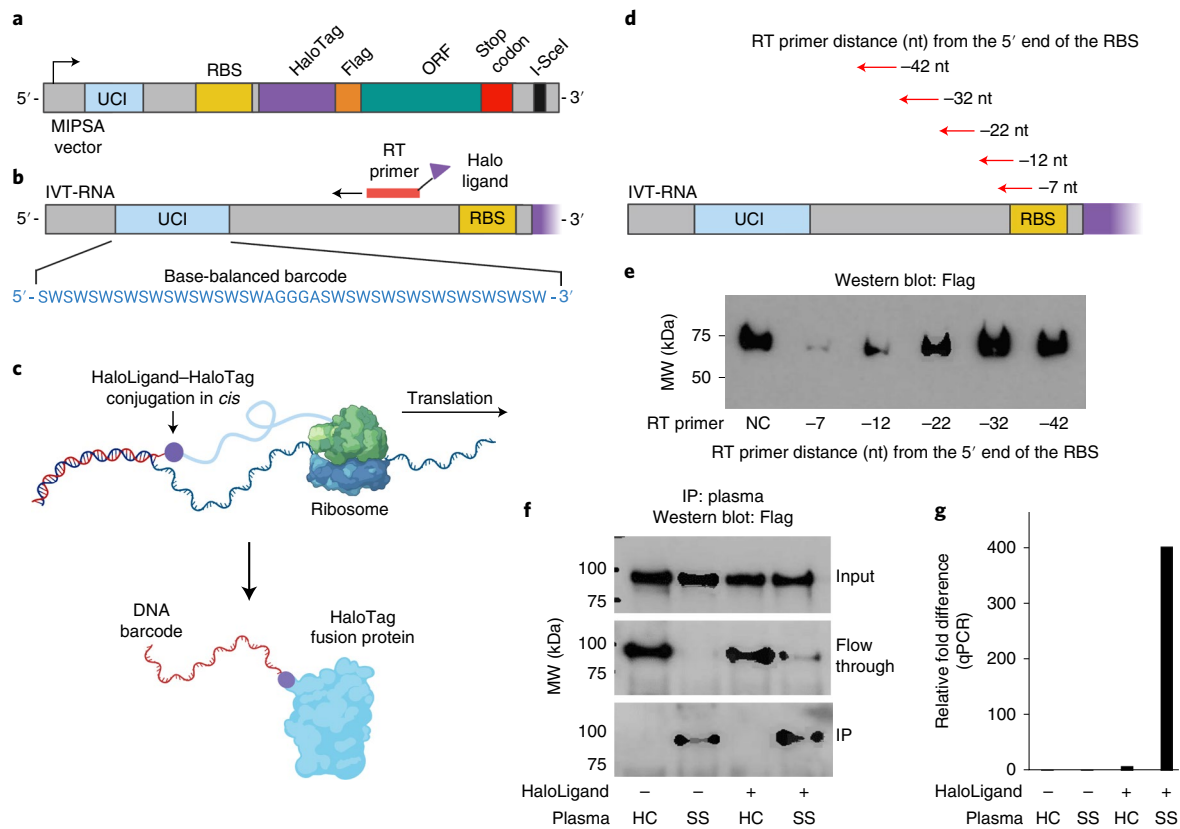


Fig. 1 | The MIPSA method. **a**, Schematic of the recombined pDEST-MIPSA vector with key components highlighted: UCI (blue), RBS (yellow), N-terminal HaloTag (purple), FLAG epitope (orange), ORF (green) and the I-SceI restriction endonuclease site (black) for vector linearization. **b**, Schematic showing IVT-RNA from the vector template shown in **a**. Isothermal base-balanced UCI sequence: (SW)₁₈-AGGGA-(SW)₁₈. **c**, Cell-free translation of the RNA-cDNA shown in **b**. HaloTag protein forms a covalent bond with the HaloLigand-conjugated UCI-containing cDNA in *cis* during translation. **d**, RT primer positions tested for impact on translation. **e**, α -FLAG western blot analysis of translation in presence of RT primers depicted in **d** (NC, negative control, no RT primer). **f**, Western blot analysis of TRIM21 protein translated from RNA carrying the UCI-cDNA primed from the -32 position, either conjugated (+) or not (-) with the HaloLigand, IPed with healthy control (HC) or Sjögren's syndrome (SS) plasma. **g**, qPCR analysis of the immunoprecipitated TRIM21 UCI. Fold difference is by comparison with the HaloLigand (-) HC IP.

clone, which was combined with a 1:1 mixture of the first GAPDH and TRIM21 clones (Fig. 2b).

Establishing and deconvoluting a stochastically barcoded human ORFeome MIPSA library. The sequence-verified human ORFeome (hORFeome) v8.1 is composed of 12,680 clonal ORFs mapping to 11,437 genes in the Gateway Entry plasmid (pDONR223)²¹. Five subpools of the library were created, each composed of ~2,500 similarly sized ORFs. Each of the five subpools was separately recombined into the pDEST-MIPSA UCI plasmid library and transformed to obtain approximately tenfold ORF coverage (~25,000 clones per subpool). Each subpool was assessed via Bioanalyzer electrophoresis, sequencing of ~20 colonies and Illumina sequencing of the combined superpool. The *TRIM21* plasmid was spiked into the superpooled hORFeome library at 1:10,000—comparable to a typical library member. The SS immunoprecipitation (IP) experiment was then performed on the hORFeome MIPSA library, using sequencing as a readout. The read counts from all UCIs in the library, including the spiked-in *TRIM21*, are shown for the SS IP versus the average of eight mock IPs in Fig. 2c. Reassuringly, the SS autoantibody-dependent enrichment of *TRIM21* (17-fold) was similar to the model system (Fig. 2d). See 'Informatic analysis of MIPSA sequencing data' in Methods for a description of the analytical pipeline for sequencing data.

Next, we established a system for creating a UCI-ORF look-up dictionary, using tagmentation and sequencing (Fig. 3a). Sequencing

the 5' 50 nt of the ORF inserts detected 11,076 of the 11,887 unique 5' 50 nt library sequences. Of the 153,161 UCIs detected, 82.9% (126,975) were found to be associated with a single ORF (termed 'monospecific UCI'). Each ORF was uniquely associated with a median of 9 (ranging from 0 to 123) monospecific UCIs (Fig. 3b). Importantly, an ensemble of monospecific UCIs with consistent behaviour can provide additional, strong support for the reactivity of their associated ORF. We noted a weak, inverse correlation between UCI number and ORF size, which most likely reflects the less efficient recombination of larger ORF-containing plasmids in the pooled recombination reactions. After aggregation of the read counts corresponding to each ORF, over 99% of the represented ORFs were present within a tenfold difference of the median ORF abundance (Fig. 3c). Taken together, these data indicate that we established a uniform library of 11,076 stochastically indexed human ORFs and defined a look-up dictionary for downstream analyses. Figure 3d shows UCI read counts of an SS IP versus the average of eight mock IPs and the 47 dictionary-decoded GAPDH monospecific UCIs (corresponding to two GAPDH isoforms present in the hORFeome library) appearing along the $y=x$ diagonal as expected. To avoid ambiguity, any UCI associated with more than a single ORF was excluded from further analyses.

Unbiased MIPSA analysis of autoantibodies associated with severe COVID-19. Several recent reports have described elevated autoantibody reactivities in patients with severe COVID-19 (refs. 22–26).

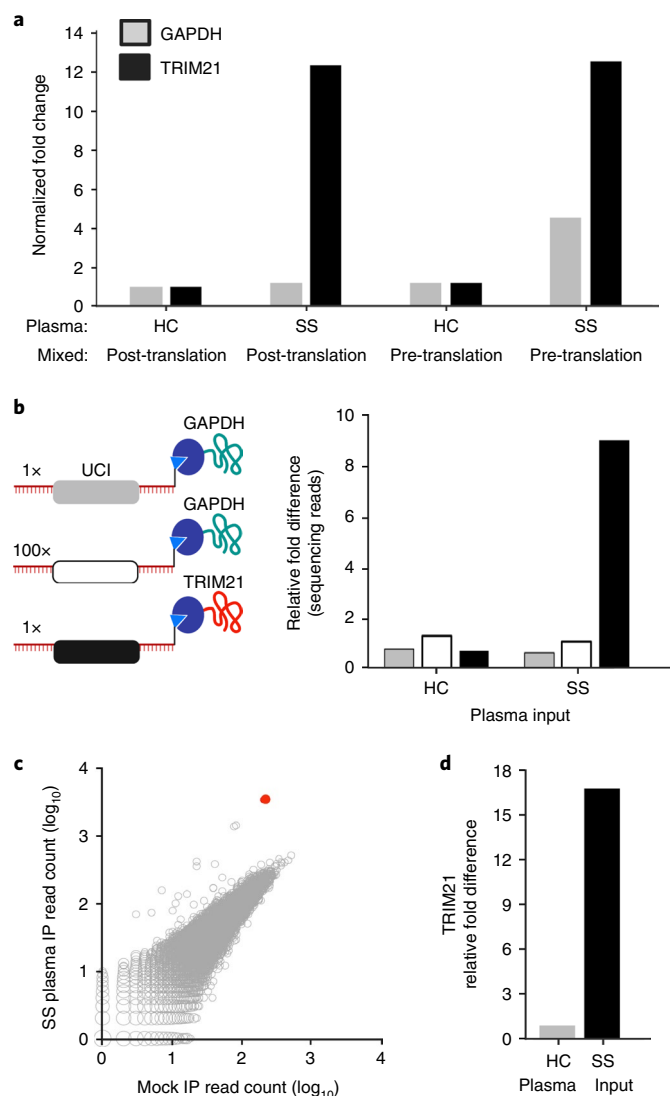


Fig. 2 | Cis- versus trans-UCI conjugation. **a**, IVT-RNA encoding TRIM21 or GAPDH with their distinct UCI barcodes was translated before or after mixing at a 1:1 ratio. qPCR analysis of the IPs using UCI-specific primers, reported as fold change versus IP with healthy control (HC) plasma, which is set to 1, when the IVT-RNA was mixed post-translation. Sjögren's syndrome, SS. **b**, IVT-RNA encoding TRIM21 (black UCI) and GAPDH (grey UCI) were mixed 1:1 into a background of 100-fold excess GAPDH (white UCI) and then translated as a mock library. Sequencing analysis of the IPs, reported as fold change versus the HC IP of the 100x GAPDH. **c**, hORFeome MIPSAs library containing spiked-in TRIM21, immunoprecipitated with SS plasma and compared with average of eight mock IPs (no plasma input). The TRIM21 UCI is shown in red. **d**, Relative fold difference of TRIM21 UCI in SS versus HC IPs, determined by sequencing.

We therefore used MIPSAs with the human ORFeome library for unbiased identification of autoreactivities in the plasma of 55 patients with severe COVID-19, defined here only on the basis of hospital admission, since the availability of clinical meta-data was incomplete. For comparison, we used MIPSAs to detect autoreactivities in plasma from ten healthy donors and ten COVID-19 convalescent plasma donors who had not been hospitalized (Supplementary Table 1). As we have done previously for phage immunoprecipitation sequencing (PhIP-seq) analyses, each sample was compared with a set of eight 'mock IPs', which contained all reaction components

except for plasma, and was run on the same plate. Comparison with mock IPs accounts for bias in the library and background binding. The informatic pipeline used to detect antibody-dependent reactivity (Methods) yielded a median of five (ranging from two to nine) false-positive UCI hits per mock IP. IPs using plasma from patients with severe COVID-19, however, yielded a mean of 83 reactive proteins among patients with severe COVID-19, which was significantly more than the mean of 64 reactive proteins among healthy pre-pandemic controls and significantly more than the mean of 62 reactive proteins among recovered individuals after mild to moderate COVID-19 ($P=0.02$ and $P=0.05$, respectively, one tailed t -test; Fig. 4a).

We next examined proteins in the severe COVID-19 IPs that had at least two reactive UCIs (in the same IP) that were reactive in at least one severe patient and that were not reactive in more than one control (healthy or mild-to-moderate convalescent plasma). Proteins were excluded if they were reactive in a single patient with severe COVID-19 and a single control. The 103 proteins that met these criteria are shown in the cluster map of Fig. 4b. Fifty-one of the 55 patients with severe COVID-19 exhibited reactivity to at least one of these proteins. We noted co-occurring protein reactivities in multiple individuals, the vast majority of which lack homology by protein sequence alignment. Supplementary Table 2 provides summary statistics about these reactive proteins, including whether they are previously defined autoantigens according to the human autoantigen database AAgAtlas 1.0 (ref. 27). Supplementary dataset provides the patient versus UCI fold change data used to construct the cluster map.

One notable autoreactivity cluster (Supplementary Table 2, cluster 5) includes 5'-nucleotidase, cytosolic 1A (NT5C1A), which is highly expressed in skeletal muscle and is the most well-characterized autoantibody target in inclusion body myositis (IBM). Multiple UCIs linked to NT5C1A were significantly increased in 3 of the 55 patients with severe COVID-19 (5.5%). NT5C1A autoantibodies have been reported in up to 70% of patients with IBM³, in ~20% of patients with SS and in up to ~5% of healthy donors.²⁸ The prevalence of NT5C1A reactivity in the severe COVID-19 cohort is therefore not necessarily elevated. However, we wondered whether MIPSAs would be able to reliably distinguish between healthy donor and IBM plasma on the basis of NT5C1A reactivity. We tested plasma from ten healthy donors and ten patients with IBM, the latter of whom were selected on the basis of NT5C1A seropositivity determined by PhIP-seq¹. The clear separation of patients from controls in this independent cohort suggests that MIPSAs may indeed have utility in clinical diagnostic testing using either UCI-specific qPCR or library sequencing, which were tightly correlated readouts (Fig. 4c).

Type-I and type-III IFN-neutralizing autoantibodies in patients with severe COVID-19. Neutralizing autoantibodies targeting type-I interferons alpha (IFN- α) and omega (IFN- ω) have been associated with severe COVID-19 (refs. 16,23,29). All type-I IFNs except IFN- α 16 are represented in the human MIPSAs ORFeome library and annotated in the look-up dictionary. IFN- α 4, IFN- α 17 and IFN- α 21 are indistinguishable by the first 50 nucleotides of their encoding ORF sequences and thus analysed as a single ORF. Two of the patients with severe COVID-19 (P1 and P2) in this cohort (3.6%) exhibited dramatic type-I IFN autoreactivity (49 and 46 type-I IFNs UCIs, across 11 distinct IFN- α and IFN- ω ORFs; Fig. 5a,b). The extensive co-reactivity of these proteins is probably attributable to their sequence homology (Supplementary Fig. 4). By requiring at least two reactive IFN UCIs to be considered positive, we identified two additional severe COVID-19 plasma samples (P3 and P4) with detectable levels of IFN- α reactivity, each with only two reactive IFN- α UCIs. Fifty percent of these four patients with autoreactive IFN- α died, versus about 30% of the remaining cohort.

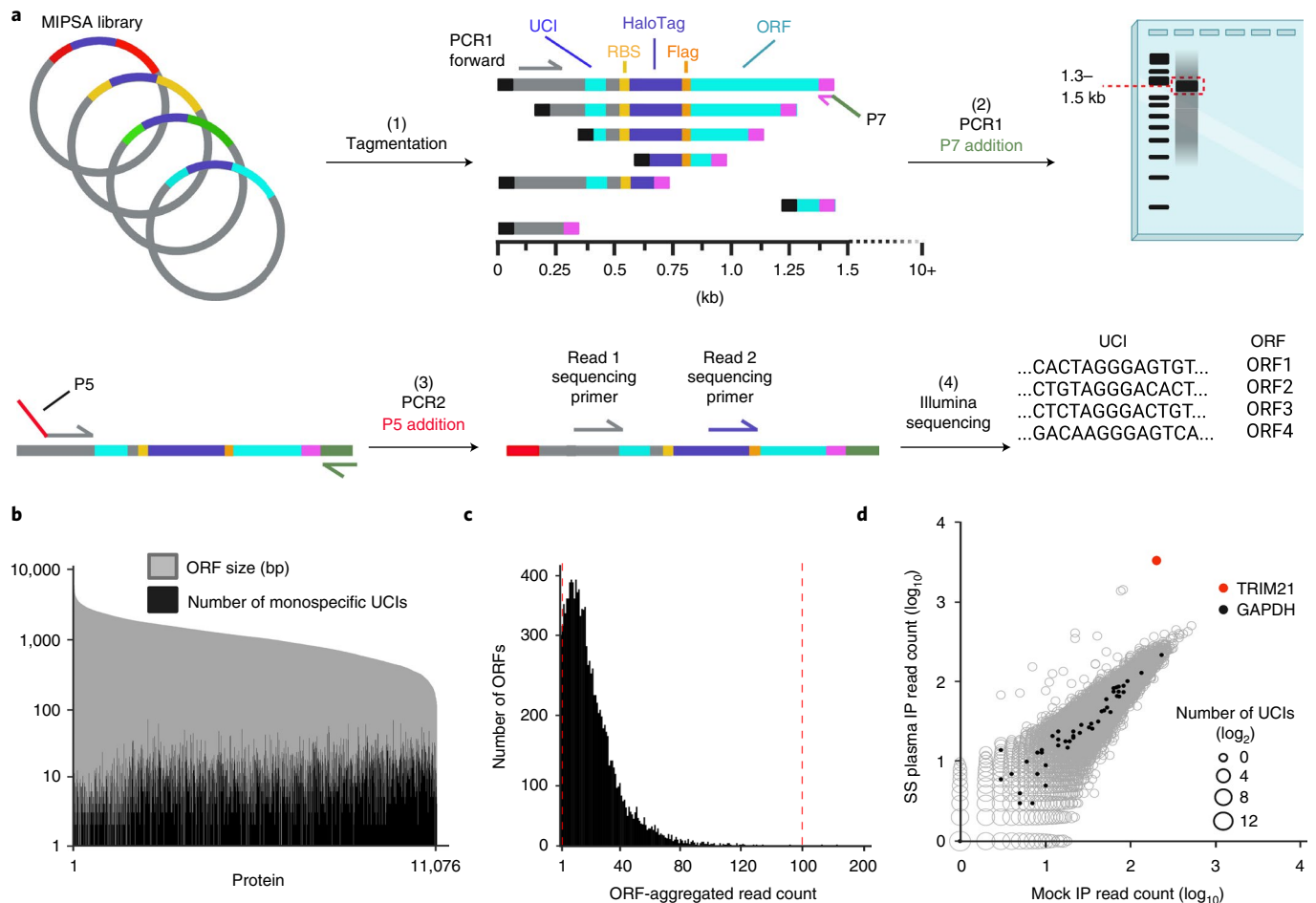


Fig. 3 | Constructing the UCI-ORF dictionary. **a**, (1) Tagmentation randomly inserts adapters into the MIPSAs vector library. (2) Using a PCR1 forward primer and the reverse primer of the tagmentation-inserted adapter, DNA fragments are amplified and size selected to be ~1.5 kb, which captures the 5' terminus of the ORF. (3) These fragments are amplified with a P5-containing PCR2 forward primer and a P7 reverse primer. (4) Illumina sequencing is used to read the UCI and the ORF from the same fragment, thus enabling their association in the dictionary. **b**, The number of monospecific UCIs is shown for each member of the pDEST-MIPSAs hORFeome library, superimposed on the length of the ORFs. **c**, Histogram of ORF representations in the library according to their aggregated UCI-associated read counts. Vertical red lines show $\pm 10\times$ the median UCI-associated read count. **d**, IP of hORFeome MIPSAs library using Sjögren's syndrome (SS) plasma is compared with the average of eight mock IPs. Sequencing read count for each UCI is plotted. UCIs associated with the two GAPDH isoforms (filled black) and spiked-in TRIM21 (red) are indicated.

Interestingly, one additional plasma sample (P5) precipitated no UCIs from any type-I or type-II IFNs, but five UCIs from the type-III IFN, IFN- $\lambda 3$ (Fig. 5c,d). This patient also died of COVID-19. No additional IFN autoreactivities were detected among the patients with severe COVID-19. None of the healthy or non-hospitalized COVID-19 controls was positive for two or more IFN UCIs.

We further assessed the performance of MIPSAs using P2 plasma, which neutralizes both type-I and type-III IFNs. MIPSAs was run on P2 plasma in triplicate, yielding a high level of assay reproducibility (Supplementary Fig. 5a,b), both in consistent detection of hits and low coefficients of variation (mean 22%). We next determined the linearity of the assay by diluting P2 plasma tenfold into healthy plasma and then performing MIPSAs again. The results demonstrate a consistent decrease in signal among the reactivities (mean of 5.4-fold for reactive IFNs) and loss of detection of some hits, particularly of ORFs with single reactive UCIs.

Incubation of A549 human adenocarcinomatous lung epithelial cells with 100 U ml^{-1} IFN- α or 1 ng ml^{-1} of IFN- $\lambda 3$ for 4 h in serum-free medium results in a robust upregulation of the IFN-response gene *MX1* by $\sim 1,000$ -fold and ~ 100 -fold, respectively. Pre-incubation of IFN- $\alpha 2$ with plasma P1, P2 or P3 completely

abolished *MX1* upregulation (Fig. 5e). The plasma with the weakest IFN- α reactivity by MIPSAs, P4, only partially neutralized the cytokine. Neither HC nor P5 plasma had any effect on the response of A549 cells to IFN- $\alpha 2$ treatment. However, pre-incubation of the IFN- $\lambda 3$ cytokine with the MIPSAs-positive plasma, P2 and P5, ablated the IFN response (Fig. 5f). None of the other plasma (HC, P1, P3 or P4) had any effect on the response of A549 cells to IFN- $\lambda 3$. By comparison against titration curves using IFN- $\alpha 2$ and IFN- $\lambda 3$ monoclonal antibodies, a serial titration using patient P2 plasma in triplicate indicated circulating levels of these autoantibodies to be $\sim 20 \mu\text{g ml}^{-1}$ and $\sim 100 \text{ ng ml}^{-1}$, respectively (Supplementary Fig. 6). MIPSAs analysis of the serially diluted IFN- $\alpha 2$ mAb revealed broad IFN- α cross-recognition but mutually exclusive binding of the monoclonal antibodies to the appropriate type-I or type-III IFN (Supplementary Fig. 7a,b). Importantly, we noted that loss of MIPSAs detection sensitivity corresponded to the same or greater plasma dilutions at which IFN- $\alpha 2$ and IFN- $\lambda 3$ neutralization activities were also lost. Finally, the titre of P2's autoantibodies exhibited at least a ten-fold preference for IFN- $\lambda 3$ neutralization over IFN- $\lambda 1$ neutralization (Supplementary Fig. 8). In summary, MIPSAs-based autoantibody profiling of this severe COVID-19 cohort identified

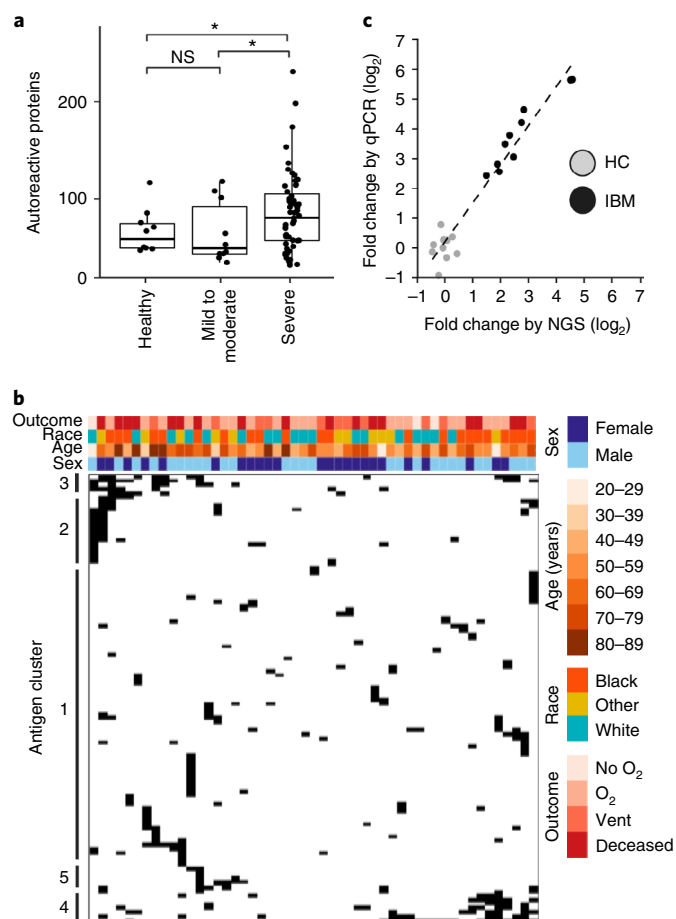


Fig. 4 | MIPSAs analysis of autoantibodies in severe COVID-19. a, Box plots showing total numbers of autoreactive proteins in plasma from healthy controls (median 69.0 ± standard deviation (s.d.) 36.3), patients with mild-to-moderate COVID-19 (60.5 ± 44.7) or patients with severe COVID-19 (106.0 ± 67.6). Boxes indicate quartiles, and asterisks indicate $P=0.02$ and $P=0.05$ from a one-tailed t -test to compare means. NS, not significant. **b**, Hierarchical cluster map of all proteins represented by at least two reactive UCIs in at least one severe COVID-19 plasma, but no more than one control (healthy or mild-to-moderate COVID-19 plasma). **c**, MIPSAs analysis of autoantibodies in ten patients with inclusion body myositis (IBM) and ten healthy controls (HC), using the hORFeome library. Fold change of immunoprecipitated NT5C1A, measured both as UCI-qPCR fold change (relative to average of ten HCs) and as sequencing fold change (relative to mock IPs).

strongly neutralizing IFN- α autoantibodies in 7.3% of patients and strongly neutralizing IFN- λ autoantibodies in 3.6% of patients, with a single patient (1.8%) harbouring both autoreactivities.

We then determined whether PhIP-seq with a 90-amino-acid (aa) human peptidome library³⁰ might also detect IFN autoantibodies in this cohort. PhIP-seq detected IFN- α reactivity in plasma from P1 and P2, although to a much lesser extent (Fig. 5g). The two weaker IFN- α reactivities detected by MIPSAs in the plasma of P3 and P4 were both missed by PhIP-seq. PhIP-seq identified a single additional weakly IFN- α reactive sample, which was negative by MIPSAs (not shown). Both technologies detected type-III IFN autoreactivity (directed exclusively at IFN- λ 3). PhIP-seq data were used to narrow the location of a dominant epitope in these type-I and type-III IFN autoantigens (Fig. 5h for IFN- α ; amino acid position 45–135 for IFN- λ 3).

We next wondered about the prevalence of the previously unreported IFN- λ 3 autoreactivity in the general population and whether

it might be increased among patients with severe COVID-19. PhIP-seq was previously used to profile the plasma of 423 HCs, none of whom was found to have detectable IFN- λ 3 autoreactivity.³¹ These data suggest that IFN- λ 3 autoreactivity is likely to be more frequent among individuals with severe COVID-19. Therefore, neutralizing IFN- λ 3 autoantibodies may be involved in a pathogenic mechanism contributing to life-threatening COVID-19 in a subset of patients.

Discussion

We have described a molecular-display technology for full-length proteins that provides key advantages over protein microarrays and alternative techniques (such as PLATO). MIPSAs uses self-assembly to produce a library of proteins, linked to relatively short (158 nt) single-stranded cDNA barcodes via the 25-kDa HaloTag domain. This compact barcoding approach will probably have many applications not accessible to alternative display formats with bulky linkage cargoes (such as yeast, bacteria, viruses, phages, ribosomes, mRNAs and cDNAs). Indeed, individually conjugating minimal DNA barcodes to proteins, especially antibodies and antigens, have already proven useful in several settings, including CITE-seq (Cellular Indexing of Transcriptomes and Epitopes by Sequencing)³², LIBRA-seq (linking B cell receptor to antigen specificity through sequencing)³³ and related methodologies³⁴. At proteome scale, MIPSAs will enable unbiased analyses of protein–antibody, protein–protein and protein–small-molecule interactions, as well as studies of post-translational modifications, such as hapten-modification studies³⁵ or protease-activity profiling³⁶. Key advantages of MIPSAs include its high throughput, low cost, simple sequencing-library preparation, inherent compatibility with PhIP-seq and the stability of the protein–DNA complexes (important for the manipulation and storage of display libraries). Importantly, MIPSAs can be adopted by standard molecular biology laboratories, since it does not require specialized training or instrumentation (but does require access to a high-throughput DNA-sequencing instrument or facility).

Autoantibodies detected in patients with severe COVID-19 using MIPSAs. Neutralizing IFN- α/ω autoantibodies have been described in patients with severe COVID-19 disease and are presumed to be pathogenic.²³ These likely pre-existing autoantibodies, which occur very rarely in the general population, block restriction of viral replication in cell culture and are thus likely to interfere with disease resolution. This discovery paved the way to identifying a subset of individuals at risk for life-threatening COVID-19 and proposed therapeutic use of IFN- β in this population of patients. In our study, MIPSAs identified two individuals with extensive reactivity to the entire family of IFN- α cytokines. Indeed, plasma from both individuals, plus two individuals with weaker IFN- α reactivity detected by MIPSAs, robustly neutralized recombinant IFN- α 2 in a lung adenocarcinomatous cell culture model.

Type-III IFNs (IFN- λ , also known as IL-28/29) are cytokines with potent anti-viral activities that act primarily at barrier sites. The IFN- λ R1/IL-10RB heterodimeric receptor for IFN- λ is expressed on lung epithelial cells and is important for the innate response to viral infection. Previous studies in mice determined that IFN- λ diminished pathogenicity and suppressed replication of influenza viruses, respiratory syncytial virus, human metapneumovirus and severe acute respiratory syndrome coronavirus (SARS-CoV-1)³⁷. It has been proposed that IFN- λ exerts much of its antiviral activity in vivo via stimulatory interactions with immune cells, rather than through induction of the antiviral cell state³⁸. However, IFN- λ has been found to robustly restrict SARS-CoV-2 replication in primary human bronchial epithelial cells³⁹, primary human airway epithelial cultures⁴⁰ and primary human intestinal epithelial cells⁴¹. Collectively, these studies suggest multifaceted

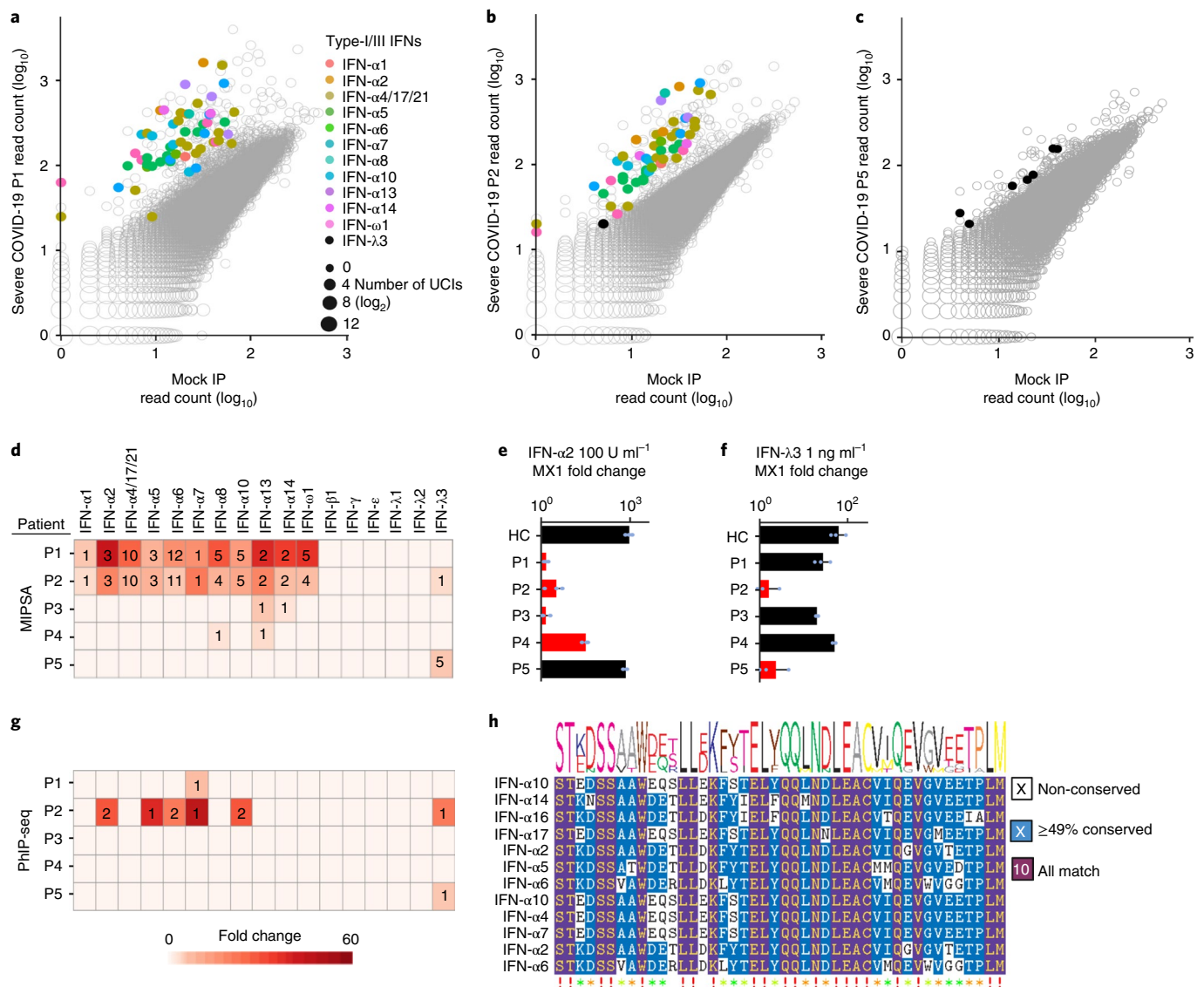


Fig. 5 | MIPSA detects known and novel neutralizing IFN autoantibodies. **a–c**, Scatterplots highlighting reactive IFN UCIs for three patients with severe COVID-19. **d**, Summary of IFN reactivity detected in 5 of 55 individuals with severe COVID-19. Hit fold-change values (colour of cell) and the number of reactive UCIs (number in cell) are provided. **e, f**, Recombinant IFN- α 2 or IFN- λ 3 neutralizing activity of the same patients shown in **d**. Plasma were pre-incubated with 100 U ml⁻¹ of IFN- α 2 or 1 ng ml⁻¹ of IFN- λ 3 before incubation with A549 cells. Fold changes of the IFN stimulated gene, *MX1*, were calculated by RT-qPCR relative to unstimulated cells ($n=3$ for each of the five patient samples). For **e**, samples labelled HC, P1, P2, P3, P4 and P5 have mean and s.d. values of 977.7 ± 253.7 , 1.39 ± 0.2 , 3.1 ± 1.8 , 1.4 ± 0.5 , 32 ± 7.2 and 741.1 ± 121 , respectively. For **f**, samples labelled HC, P1, P2, P3, P4 and P5 have mean and s.d. values of 64.5 ± 26.8 , 28.2 ± 12.1 , 1.6 ± 1.0 , 20.3 ± 1.4 , 52.4 ± 5.1 and 2.3 ± 2.0 , respectively. *GAPDH* was used as a housekeeping control gene for normalization. Red bars indicate which samples were found to contain the corresponding anti-IFN antibodies using MIPSA. **g**, PhIP-seq analysis of IFN autoantibodies in the five patients of **d** (row and column orders maintained). Hit fold-change values (colour of cell) and the number of reactive peptides (number in cell) are provided. **h**, Epitopefinder analysis of the PhIP-seq reactive type-I IFN 90-aa peptides.

mechanisms by which neutralizing IFN- λ autoantibodies may exacerbate SARS-CoV-2 infections.

Among 55 patients with severe COVID-19, MIPSA detected two individuals with IFN- λ 3 reactive autoantibodies. The same autoreactivities were also detected using PhIP-seq. We tested the IFN- λ 3 neutralizing capacity of these patients' plasma, observing near-complete ablation of the cellular response to the recombinant cytokine (Fig. 5f). These data suggest that IFN- λ 3 autoreactivity is a potentially pathogenic mechanism contributing to severe COVID-19 disease.

In one study, type-III IFN neutralizing antibodies were not detected among a cohort of 101 individuals with type-I IFN autoantibodies tested.²³ In our study, one of the four IFN- α autoreactive

individuals (P2, a 22-year-old male) also harboured autoantibodies that neutralized IFN- λ 3. It is possible that this co-reactivity is extremely rare and thus not represented in the aforementioned 101-patient study. Alternatively, it is possible that the differing assay conditions exhibit different detection sensitivity. Whereas in the previous study cultured A549 cells were incubated with IFN- λ 3 at 50 ng ml⁻¹ without plasma pre-incubation, we cultured A549 cells with IFN- λ 3 at 1 ng ml⁻¹ after pre-incubation with plasma for 1 h. Their readout of STAT3 phosphorylation may also provide different detection sensitivity compared with the upregulation of *MX1* expression. A larger study is needed to determine the true frequency of these reactivities in patients with severe COVID-19 and matched controls. Here, we report detection of strongly neutralizing IFN- α

and IFN- λ 3 autoantibodies in 4 (7.3%) and 2 (3.6%) individuals, respectively, in a cohort of 55 patients with severe COVID-19. IFN- λ 3 autoantibodies were not detected via PhIP-seq in a larger cohort of 423 HCs collected before the pandemic.

Exogenously administered type-III IFNs have been proposed as a therapeutic for SARS-CoV-2 infection^{40,42–46}, and there are currently three ongoing clinical trials to test PEGylated IFN- λ 1 for efficacy in reducing morbidity and mortality associated with COVID-19 (ClinicalTrials.gov Identifiers [NCT04343976](#), [NCT04534673](#) and [NCT04344600](#)). One recently completed double-blind, placebo-controlled trial, [NCT04354259](#), reported a significant reduction by 2.42 log copies per millilitre of SARS-CoV-2 at day 7 among patients with mild-to-moderate COVID-19 in the outpatient setting ($P=0.0041$)⁴⁷. Future studies will determine whether anti-IFN- λ 3 autoantibodies are pre-existing or arise in response to SARS-CoV-2 infection and how often they also cross-neutralize IFN- λ 1. On the basis of neutralization data from P2 (Supplementary Fig. 8) and sequence alignment of IFN- λ 1 and IFN- λ 3 (~29% homology, Supplementary Fig. 4), cross-neutralization is expected to be rare, raising the possibility that patients with neutralizing IFN- λ 3 autoantibodies may derive benefit from PEGylated IFN- λ 1 treatment.

While clusters of uncharacterized autoreactivities were observed in multiple individuals, it is not clear what role, if any, they may play in severe COVID-19. In larger-scale studies, we expect that patterns of co-occurring reactivity, or reactivities towards proteins with related biological functions, may ultimately define new autoimmune syndromes associated with severe COVID-19.

Complementarity of MIPSA and PhIP-seq. Display technologies frequently complement one another but may not be amenable to routine simultaneous use. MIPSA is more likely than PhIP-seq to detect antibodies directed at conformational epitopes on proteins expressed well in vitro. This was exemplified by the robust detection of IFN- α autoantibodies via MIPSA, which were less sensitively detected via PhIP-seq. PhIP-seq, on the other hand, is more likely to detect antibodies directed at less conformational epitopes contained within proteins that are either absent from an ORFeome library or cannot be expressed well in cell-free lysate. Because MIPSA and PhIP-seq naturally complement one another in these ways, we designed the MIPSA UCI amplification primers to be the same as those we have used for PhIP-seq. As the UCI–protein complex is stable—even in phage preparations—MIPSA and PhIP-seq can readily be performed together in a single reaction, using a single set of amplification and sequencing primers. The compatibility of these two display modalities lowers the barrier to leveraging their synergy.

Variations of the MIPSA system. A key aspect of MIPSA involves the conjugation of a protein to its associated UCI in *cis*, compared with another library member's UCI in *trans*. Here, we have used covalent conjugation via the HaloTag/HaloLigand system, but others could work as well. For instance, the SNAP-tag (a 20 kDa mutant of the DNA repair protein O⁶-alkylguanine-DNA alkyltransferase) forms a covalent bond with benzylguanine (BG) derivatives⁴⁸. BG could thus be used to label the RT primer in place of the HaloLigand. A mutant derivative of the SNAP-tag, the CLIP-tag, binds O₂-benzylcytosine derivatives, which could also be adapted to MIPSA⁴⁹.

The rate of HaloTag maturation and ligand binding is critical to the relative yield of *cis* versus *trans* UCI conjugation. A previous study determined that the rate of HaloTag protein production is about fourfold higher than the rate of HaloTag functional maturation⁵⁰. Considering a typical protein size is <1,000 amino acids in the ORFeome library, these data predict that most proteins should be released from the ribosome before HaloTag maturation, and

thus before *cis* HaloLigand conjugation could occur, thereby favoring unwanted *trans* barcoding. However, we observed ~50% of protein–UCI conjugates are formed in *cis*, thereby enabling excellent assay performance in the setting of a complex library. During optimization experiments, we found the rate of *cis* barcoding to be slightly improved by excluding release factors from the translation mix, which stalls ribosomes on their stop codons and allows HaloTag maturation to continue in proximity to its UCI. Alternative approaches to promote controlled ribosomal stalling could include stop codon removal/suppression or use of a dominant negative release factor. Ribosome release could then be induced via addition of the chain terminator puromycin.

Since UCI cDNAs are formed on the 5' UTR of the IVT-RNA, eukaryotic ribosomes would be unable to scan from the 5' cap to the initiating Kozak sequence. The MIPSA system described here is therefore incompatible with cap-dependent eukaryotic cell-free translation systems. If cap-dependent translation is desired, however, two alternative methods could be developed. First, the current 5' UCI system could be used if an internal ribosome entry site were to be placed between the RT primer and the Kozak sequence. Second, the UCI could instead be introduced at the 3' end of the RNA, provided that the RT was prevented from extending into the ORF. In an extension of eukaryotic MIPSA, RNA–cDNA hybrids could potentially be transfected into living cells or tissues, where UCI–protein formation could take place in situ, enabling many additional applications.

The ORF-associated UCIs can be embodied in a variety of ways. Here, we have stochastically assigned indexes to the human ORFeome at ~10⁶ representation. This approach has two main benefits: first, a single degenerate oligonucleotide pool is low cost; second, multiple independent measurements are reported by the ensemble of UCIs associated with each ORF. We have designed our library of UCIs with uniform GC content and, thus, uniform PCR amplification efficiency. For simplicity, we have opted not to incorporate unique molecular identifiers into the RT primer, but this approach is compatible with MIPSA UCIs and may potentially enhance quantitation. One disadvantage of stochastic indexing is the potential for ORF dropout and, thus, the need for relatively high UCI representation; this increases the depth of sequencing required to quantify each UCI and, thus, the overall per-sample cost. A second disadvantage is the requirement to construct a UCI–ORFeome matching dictionary. With short-read sequencing, we were unable to disambiguate a fraction of the library, composed mostly of alternative isoforms. Using a long-read sequencing technology, such as PacBio or Oxford Nanopore Technologies, instead of or in addition to short-read sequencing technology could surmount incomplete disambiguation. As opposed to stochastic barcoding, individual UCI–ORF cloning is possible but costly and cumbersome. However, a smaller UCI set would provide the advantage of lower per-assay sequencing cost. We have previously developed a methodology to clone ORFeomes using Long Adapter Single Stranded Oligonucleotide (LASSO) probes⁵¹. LASSO cloning of ORFeome libraries thus naturally synergizes with MIPSA-based applications.

MIPSA readout via qPCR. A useful feature of appropriately designed UCIs is that they can also serve as qPCR readout probes. The degenerate UCIs that we have designed and used here (Fig. 1b) comprise 18 nt base-balanced forward and reverse primer binding sites. The low cost and rapid turnaround time of a qPCR assay can thus be leveraged in combination with MIPSA. For example, incorporating assay quality-control measures, such as TRIM21 IP, can be used to qualify a set of samples before a costlier sequencing run. Troubleshooting and optimization can similarly be expedited by employing qPCR as a readout, rather than relying exclusively on next-generation DNA sequencing (NGS). qPCR testing of specific UCIs may theoretically also provide enhanced sensitivity

compared with sequencing and may be more amenable to analysis in a clinical setting.

Outlook. MIPSA is a protein-display technology that has key advantages over alternative approaches. It has properties that complement techniques such as PhIP-seq, and the MIPSA ORFeome libraries can be conveniently screened in the same reactions with phage-display libraries. The MIPSA protocol requires cap-independent cell-free translation, but future adaptations may overcome this limitation. Applications for MIPSA-based studies include protein-protein, protein-antibody and protein-small-molecule interaction studies, as well as analyses of post-translational modifications. We used MIPSA to detect known autoantibodies and to discover neutralizing IFN- λ 3 autoantibodies, among many other potentially pathogenic autoreactivities (Supplementary Table 2) that may contribute to life-threatening COVID-19 in a subset of at-risk individuals.

Methods

MIPSA destination vector construction. The MIPSA vector was constructed using the Gateway pDEST15 vector as a backbone. A gBlock fragment (Integrated DNA Technologies) encoding the RBS, Kozak sequence, N-terminal HaloTag fusion protein and FLAG tag, followed by an attR1 sequence, was cloned into the parent plasmid. A 150bp poly(A) sequence was also added after attR2 site. The *TRIM21* and *GAPDH* ORF sequences used for characterizing and optimizing the two-component system included native stop codons that were retained in the final MIPSA construct.

UCI barcode library construction. A 41 nt barcode oligo was generated within a gBlock Gene Fragment (Integrated DNA Technologies) with alternating mixed bases (S: G/C; W: A/T) to produce the following sequence: (SW)₁₈-AGGGA-(SW)₁₈. The sequences flanking the degenerate barcode incorporated the standard PhIP-seq PCR1 and PCR2 primer binding sites³². Eighteen nanograms of the starting UCI library was used to run 40 cycles of PCR to amplify the library and incorporate BglII and PspXI restriction sites. The MIPSA vector and amplified UCI library were then digested with the restriction enzymes overnight, column purified and ligated at 1:5 vector-to-insert ratio. The ligated MIPSA vector was used to transform electrocompetent One Shot ccdB 2 T1^R cells (Thermo Fisher Scientific). Six transformation reactions yielded ~800,000 colonies to produce the pDEST-MIPSA UCI library.

Human ORFeome recombination into the pDEST-MIPSA UCI plasmid library. A total of 150 ng of each pENTR-hORFeome subpool (L1-L5) from hORFeome v8.1 was individually combined with 150 ng of the pDEST-MIPSA UCI library plasmid and 2 μ l of Gateway LR Clonase II mix (Life Technologies) for a total reaction volume of 10 μ l. The reaction was incubated overnight at 25 °C. The entire reaction was transformed into 50 μ l of One Shot OmniMAX 2 T1^R chemical competent *E. coli* (Life Technologies). In aggregate, the transformations yielded ~120,000 colonies, which is approximately tenfold the complexity of the hORFeome v8.1. Colonies were collected and pooled by scraping, followed by purification of the barcoded pDEST-MIPSA hORFeome plasmid DNA (human ORFeome MIPSA library) using the Qiagen Plasmid Midi Kit (Qiagen). The human hORFeome v8.1 collection was cloned without stop codons; the displayed proteins may therefore contain poly-lysine C-termini resulting from translation of the polyA tail. A more recent version of the MIPSA destination vector includes a stop codon in frame with recombined ORFs.

HaloLigand conjugation to RT oligo and HPLC purification. One-hundred micrograms of a 5' amine modified oligo HL-32_ad (Supplementary Table 3) was incubated with 75 μ l (17.85 μ g μ l⁻¹) of the HaloTag succinimidyl ester (O₂) (Promega Corporation), the HaloLigand, in 0.1 M sodium borate buffer for 6 h at room temperature following ref.²⁰. Then, 3 M NaCl and ice-cold ethanol was added at 10% (v/v) and 250% (v/v), respectively, to the labelling reaction and incubated overnight at -80 °C. The reaction was centrifuged for 30 min at 12,000g. The pellet was rinsed once in ice-cold 70% ethanol and air dried for 10 min.

HaloLigand-conjugated RT primer was HPLC purified using a Brownlee Aquapore RP-300 7U, 100 \times 4.6 mm column (Perkin Elmer) using a two-buffer gradient of 0-70% CH₃CN/MeCN (100 mM triethylamine acetate to acetonitrile) over 70 min. Fractions corresponding to labelled oligo were collected and lyophilized (Supplementary Fig. 1). Oligos were resuspended at 1 μ M (15.4 ng μ l⁻¹) and stored at -80 °C.

MIPSA library IVT-RNA preparation. The human ORFeome MIPSA library plasmid (4 μ g) was linearized with I-SceI restriction endonuclease (New England Biolabs) overnight. The product was column purified with the NucleoSpin Gel and PCR Clean Up Kit (Macherey-Nagel). A 40 μ l in vitro transcription reaction using the HiScribe T7 High Yield RNA Synthesis Kit (New England Biolabs)

was used to transcribe 1 μ g of the purified, linearized pDEST-MIPSA plasmid library. The product was diluted with 60 μ l molecular biology grade water, and 1 μ l of DNase I was added. The reaction was incubated for another 15 min at 37 °C. Then 50 μ l of 1 M LiCl was added to the solution and incubated at -80 °C overnight. A centrifuge was cooled to 4 °C, and the RNA was spun at maximum speed for 30 min. The supernatant was removed, and the RNA pellet washed with 70% ethanol. The sample was spun down at 4 °C for another 10 min, and the 70% ethanol removed. The pellet was dried at room temperature for 15 min and subsequently resuspended in 100 μ l water. To preserve the sample, 1 μ l of 40 U μ l⁻¹ RNaseOUT Recombinant Ribonuclease Inhibitor (Life Technologies) was added.

MIPSA library IVT-RNA RT and translation. An RT reaction was prepared using SuperScript IV First-Strand Synthesis System (Life Technologies). First, 1 μ l of 10 mM dNTPs, 1 μ l of RNaseOUT (40 U μ l⁻¹), 4.17 μ l of the RNA library (1.5 μ M) and 7.83 μ l of the HaloLigand-conjugated RT primer (1 μ M, Supplementary Table 3) were combined in a single 14 μ l reaction and incubated at 65 °C for 5 min followed by a 2-min incubation on ice. Four microlitres of 5 \times RT buffer, 1 μ l of 0.1 M dithiothreitol and 1 μ l of SuperScript IV RT Enzyme (200 U μ l⁻¹) were added to the 14 μ l reaction on ice and incubated for 20 min at 42 °C. A single 20 μ l RT reaction received 36 μ l of RNAClean XP beads (Beckman Coulter) and was incubated at room temperature for 10 min. The beads were collected by magnet and washed five times with 70% ethanol. The beads were air dried for 10 min at room temperature and resuspended in 7 μ l of 5 mM Tris-HCl, pH 8.5. The product was analysed with spectrophotometry to measure the RNA yield. A translation reaction was set up on ice using the PURExpress Δ Ribosome Kit (New England Biolabs)³³. The reaction was modified such that the final concentration of ribosomes was 0.3 μ M. For each 10 μ l translation reaction, 4.57 μ l of the RT reaction was added to 4 μ l Solution A, 1.2 μ l Factor Mix and 0.23 μ l ribosomes (13.3 μ M). This reaction was incubated at 37 °C for 2 h, diluted to a total volume of 45 μ l with 35 μ l 1 \times PBS and used immediately or stored at -80 °C after addition of glycerol to a final concentration of 25% (v/v).

IP of the translated MIPSA hORFeome library. Five microlitres of plasma, diluted 1:100 in PBS, is mixed with the 45 μ l of diluted MIPSA library translation reaction (see above) and incubated overnight at 4 °C with gentle agitation. For each IP, a mixture of 5 μ l of Protein A Dynabeads and 5 μ l of Protein G Dynabeads (Life Technologies) was washed three times in two times their original volume with 1 \times PBS. The beads were then resuspended in 1 \times PBS at their original volume and added to each IP. The antibody capture proceeded for 4 h at 4 °C. Beads were collected on a magnet and washed three times in 1 \times PBS, changing tubes or plates between washes. The beads were then collected and resuspended in a 20 μ l PCR master mix containing the T7-Pep2_PCR1_F forward and the T7-Pep2_PCR1_R + ad_min reverse primers (Supplementary Table 3) and Herculase-II (Agilent). PCR cycling was as follows: an initial denaturing and enzyme activation step at 95 °C for 2 min, followed by 20 cycles of 95 °C for 20 s, 58 °C for 30 s and 72 °C for 30 s. The final extension step was performed at 72 °C for 3 min. Two microlitres of the PCR1 amplification product was used as input to a 20 μ l dual-indexing PCR reaction with the PhIP_PCR2_F forward and the PhIP_PCR2_R reverse primers, each containing 10 nt barcodes (i5 and i7, respectively). PCR cycling was as follows: an initial denaturing step at 95 °C for 2 min, followed by 20 cycles of 95 °C for 20 s, 58 °C for 30 s and 72 °C for 30 s. The final extension step was performed at 72 °C for 3 min. i5/i7 indexed libraries were pooled and column purified (NucleoSpin columns, Takara). Libraries were sequenced on an Illumina NextSeq 500 using a 1 \times 50 nt SE or 1 \times 75 nt SE protocol. MIPSA_i5_NextSeq_SP and Standard_i7_SP primers were used for i5/i7 sequencing (Supplementary Table 3). The output was demultiplexed using i5 and i7 without allowing any mismatches.

For quantification of MIPSA experiments by qPCR, the PCR1 product (above) was analysed as follows. A total of 4.6 μ l of 1:1,000 dilution of the PCR1 reaction was added to 5 μ l of Brilliant III Ultra Fast 2 \times SYBR Green Mix (Agilent), 0.2 μ l of 2 μ M reference dye and 0.2 μ l of 10 μ M forward and reverse primer mix (specific to the target UCI). PCR cycling was as follows: an initial denaturing step at 95 °C for 2 min, followed by 45 cycles of 95 °C for 20 s and 60 °C for 30 s. Following completion of thermocycling, amplified products were subjected to melt-curve analysis. The qPCR primers for MIPSA IP experiments were BT2_F and BT2_R for TRIM21, BG4_F and BG4_R for GAPDH and NT5C1A_F and NT5C1A_R for NT5C1A (Supplementary Table 3).

Plasma samples. All samples were collected from subjects who met protocol eligibility criteria, as described below. All studies protected the rights and privacy of the study participants and were approved by their respective institutional review boards for original sample collection and subsequent analyses.

Pre-pandemic and HC plasma samples. All human samples were collected before 2017 at the National Institutes of Health (NIH) Clinical Center under the Vaccine Research Center's (VRC)/National Institutes of Allergy and Infectious Diseases (NIAID)/NIH protocol 'VRC 000: Screening Subjects for HIV Vaccine Research Studies' (NCT00031304) in compliance with NIAID institutional review board-approved procedures.

COVID-19 convalescent plasma from non-hospitalized patients. Eligible non-hospitalized COVID-19 convalescent plasma donors were contacted by study personnel, as previously described³⁴. All donors were at least 18 years old and had a confirmed diagnosis of SARS-CoV-2 by detection of RNA in a nasopharyngeal swab sample. Basic demographic information (age, sex, race and hospitalization with COVID-19) was obtained from each donor; initial diagnosis of SARS-CoV-2 and date of diagnosis were confirmed by medical chart review.

Severe COVID-19 plasma samples. The study cohort was defined as inpatients who had (1) a confirmed RNA diagnosis of COVID-19 from a nasopharyngeal swab sample, (2) survival to death or discharge and (3) remnant specimens in the Johns Hopkins COVID-19 Remnant Specimen Biorepository, an opportunity sample that includes 59% of Johns Hopkins Hospital patients with COVID-19 and 66% of patients with length of stay ≥ 3 days^{55,56}. Patient outcomes were defined by the World Health Organization COVID-19 disease severity scale. Samples from patients with severe COVID-19 that were included in this study were obtained from 17 patients who died, 13 who recovered after being ventilated, 22 who required oxygen to recover and 3 who recovered without supplementary oxygen. This study was approved by the Johns Hopkins University institutional review board (IRB00248332 and IRB00273516), with a waiver of consent because all specimens and clinical data were de-identified by the Core for Clinical Research Data Acquisition of the Johns Hopkins Institute for Clinical and Translational Research; the study team had no access to identifiable patient data.

SS and IBM plasma samples. SS samples were collected under protocol NA_00013201. All patients were >18 years old and gave informed consent. Samples from patients with IBM were collected under protocol IRB00235256. All patients met ENMC 2011 diagnostic criteria³⁷ and provided informed consent.

Immunoblot analysis. Laemmli buffer containing 5% β -mercaptoethanol was added to samples, boiled for 5 min and analysed on NuPage 4–12% Bis-Tris polyacrylamide gels (Life Technologies). Following transfer to PVDF membranes, blots were blocked in 20 mM Tris-buffered saline, pH 7.6, containing 0.1% Tween 20 (TBST) and 5% (wt/vol) non-fat dry milk for 30 min at room temperature. Blots were subsequently incubated overnight at 4°C with primary anti-FLAG antibody (#F3165, MilliporeSigma) at 1:2,000 (v/v), followed by a 4-h incubation at room temperature in anti-mouse IgG, HRP-linked secondary antibody (#7076, Cell Signaling) at 1:4,000 (v/v).

Construction of the UCI-ORF dictionary. The Nextera XT DNA Library Preparation kit (Illumina) was used for tagmentation of 150 ng of the pDEST-MIPSA hORFeome plasmid library to yield the optimal size distribution centred around 1.5 kb. Tagmented libraries were amplified using Herculase-II (Agilent) with T7-Pep2_PCR1_F forward and Nextera Index 1 Read primer. PCR cycling was as follows: an initial denaturing step at 95°C for 2 min, followed by 30 cycles of 95°C for 20 s, 53.5°C for 30 s and 72°C for 30 s. A final extension step was performed at 72°C for 3 min. PCR reactions were run on a 1% agarose gel followed by excision of ~1.5 kb products and purification using the NucleoSpin Gel and PCR Clean-up columns (Macherey-Nagel). The purified product was then amplified for another ten cycles with PhIP_PCR2_F forward and P7.2 reverse primers (for a list of primer sequences, see Supplementary Table 3). The product was gel purified and sequenced on a MiSeq (Illumina) using the T7-Pep2.2_SP_subA primer for read 1 and the MISEQ_MIPSA_R2 primer for read 2. Read 1 was 60 bp long to capture the UCIs. The first index read, I1, was substituted with a 50 bp read into the ORF. I2 was used to identify the i5 index for sample demultiplexing.

The hORFeome v8.1 DNA sequences were truncated to the first 50 nt, and the ORF names corresponding to non-unique sequences were concatenated with a ‘|’ delimiter. The demultiplexed output of the 50 nt R2 (ORF) read from an Illumina MiSeq was aligned to the truncated human ORFeome v8.1 library using the Rbowtie2 package with the following parameters: options = ‘-a —very-sensitive-local’⁵⁸. The unique FASTQ identifiers were then used to extract corresponding sequences from the 60 bp R1 (UCI) read. Those sequences were then trimmed using the 3’ anchor ACGATA, and sequences that did not have the anchor were removed. Additionally, any trimmed R1 sequences that had fewer than 18 nucleotides were removed. The ORF sequences that still had a corresponding UCI post-filtering were retained using the FASTQ identifier. The names of ORFs that had the same UCI were concatenated with a ‘&’ delimiter, and this final dictionary was used to generate a FASTA alignment file composed of ORF names and UCI sequences.

Informatic analysis of MIPSA sequencing data. Illumina output FASTQ files were trimmed using the constant ACGAT anchor sequence following all UCI sequences. Next, perfect match alignment was used to map the trimmed sequences to their linked ORFs via the UCI-ORF look-up dictionary. A read count matrix was constructed, in which rows correspond to individual UCIs and columns correspond to samples. We next used the edgeR software package⁵⁹, which, using a negative binomial model, compares the signal detected in each sample against a set of negative control (‘mock’) IPs that were performed without plasma, to return a fold-change estimate and a test statistic for each UCI in every sample, thus creating

fold-change and $-\log_{10}P$ matrices. By comparison of EdgeR output data from replicate IPs, we established that significantly enriched UCIs (‘hits’) should require a read count of at least 15, a P value less than 0.001 and a fold change of at least 3. Hit fold-change matrices report the fold-change value for ‘hits’ and report a ‘1’ for UCIs that are not hits.

Protein sequence similarity. To evaluate sequence homology among proteins in the hORFeome v8.1 library, a blastp alignment was used to compare each protein sequence against all other library members (parameters ‘-outfmt 6 -evalue 100 -max_hsps 1 -soft_masking false -word_size 7 -max_target_seqs 100000’). To evaluate sequence homology among reactive peptides in the human 90-aa phage display library, the epitopefinder ([brandonsie.github.io/epitopefinder](https://github.com/brandonsie/epitopefinder)) software was employed.

PhIP-seq analyses. PhIP-seq was performed according to a previously published protocol.³² Briefly, 0.2 μ l of each plasma was individually mixed with the 90-aa human phage library and immunoprecipitated using protein-A- and protein-G-coated magnetic beads. A set of six to eight mock IPs (no plasma input) were run on each 96-well plate. Magnetic beads were resuspended in PCR master mix and subjected to thermocycling. A second PCR reaction was employed for sample barcoding. Amplicons were pooled and sequenced on an Illumina NextSeq 500 instrument using a 1 \times 50 nt SE or 1 \times 75 nt SE protocol. PhIP-seq with the human library was used to characterize autoantibodies in a collection of plasma from HCs. For fair comparison with the severe COVID-19 cohort, we first determined the minimum sequencing depth that would have been required to detect the IFN- λ 3 reactivity in both of the positive individuals. We then considered only the 423 datasets from the healthy cohort with sequencing depth greater than this minimum threshold. None of these 423 individuals was found to be reactive to any peptide from IFN- λ 3.

Type-I/III IFN neutralization assay. IFN- α 2 (catalogue no. 11100-1), IFN- λ 1 (catalogue no. 1598-IL-025) and IFN- λ 3 (catalogue no. 5259-IL-025) were purchased from R&D Systems. Twenty microlitres of plasma were incubated for 1 h at room temperature with either 100 U ml⁻¹ IFN- α 2 or 1 ng ml⁻¹ IFN- λ 3, and 180 μ l DMEM in a total volume of 200 μ l before addition into 7.5 \times 10⁴ A549 cells in 48-well tissue culture plates. After 4-h incubation, the cells were washed with 1 \times PBS and cellular mRNA was extracted and purified using RNeasy Plus Mini Kit (Qiagen). Six hundred nanograms of extracted mRNA was reverse transcribed using the SuperScript III First-Strand Synthesis System (Life Technologies) and diluted tenfold for qPCR analysis on a QuantStudio 6 Flex System (Applied Biosystems). PCR consisted of 95°C for 3 min, followed by 45 cycles of the following: 95°C for 15 s and 60°C for 30 s. *MX1* expression was chosen as a measure of cell stimulation by the IFNs, and the relative mRNA expression was normalized to *GAPDH* expression. The qPCR primers for *GAPDH* and *MX1* were obtained from Integrated DNA Technologies (Supplementary Table 3). Anti-hIFN- α 2-IgG (catalogue no. mabg-hifna-3) and anti-hIL-28b-IgG (catalogue no. mabg-hil28b-3) were purchased from InvivoGen. Manufacturer’s note about mabg-hifna-3: ‘This antibody reacts with hIFN- α 1, hIFN- α 2, hIFN- α 5, hIFN- α 8, hIFN- α 14, hIFN- α 16, hIFN- α 17 and hIFN- α 21; it reacts very weakly with hIFN- α 4 and IFN- α 10; it does not react with hIFN- α 6 or hIFN- α 7’. The manufacturer’s note about mabg-hil28b-3: ‘Reacts with human IL-28A and human IL-28B’.

Reporting summary. Further information on research design is available in the Nature Research Reporting Summary linked to this article.

Data availability

The data supporting the results in this study are available within the paper and its Supplementary Information. The raw and analysed datasets are available from the corresponding author on request. Source data are provided with this paper.

Code availability

The MIPSAAlign package for alignment and UCI-ORF matching, implemented in R v 4.0.2, is available on GitHub at <https://github.com/jgunn123/MIPSAAlign>.

Received: 7 May 2021; Accepted: 14 July 2022;

Published online: 19 August 2022

References

- Larman, H. B. et al. Cytosolic 5’-nucleotidase 1A autoimmunity in sporadic inclusion body myositis. *Ann. Neurol.* **73**, 408–418 (2013).
- Xu, G. J. et al. Viral immunology. Comprehensive serological profiling of human populations using a synthetic human virome. *Science* **348**, aaa0698 (2015).
- Shrock, E. et al. Viral epitope profiling of COVID-19 patients reveals cross-reactivity and correlates of severity. *Science* <https://doi.org/10.1126/science.abd4250> (2020).
- Monaco, D. R. et al. Profiling serum antibodies with a pan allergen phage library identifies key wheat allergy epitopes. *Nat. Commun.* **12**, 379 (2021).

5. Venkataraman, T. et al. Analysis of antibody binding specificities in twin and SNP-genotyped cohorts reveals that antiviral antibody epitope selection is a heritable trait. *Immunity* **55**, 174–184.e5 (2022).
6. Kingsmore, S. F. Multiplexed protein measurement: technologies and applications of protein and antibody arrays. *Nat. Rev. Drug Discov.* **5**, 310–320 (2006).
7. Kodadek, T. Protein microarrays: prospects and problems. *Chem. Biol.* **8**, 105–115 (2001).
8. Ramachandran, N., Hainsworth, E., Demirkan, G. & LaBaer, J. On-chip protein synthesis for making microarrays. *Methods Mol. Biol.* **328**, 1–14 (2006).
9. Rungpragayphan, S., Yamane, T. & Nakano, H. SIMPLEX: single-molecule PCR-linked in vitro expression: a novel method for high-throughput construction and screening of protein libraries. *Methods Mol. Biol.* **375**, 79–94 (2007).
10. Zhu, J. et al. Protein interaction discovery using parallel analysis of translated ORFs (PLATO). *Nat. Biotechnol.* **31**, 331–334 (2013).
11. Liszczak, G. & Muir, T. W. Nucleic acid-barcoding technologies: Converting DNA sequencing into a broad-spectrum molecular counter. *Angew. Chem. Int. Ed. Engl.* **58**, 4144–4162 (2019).
12. Los, G. V. et al. HaloTag: a novel protein labeling technology for cell imaging and protein analysis. *ACS Chem. Biol.* **3**, 373–382 (2008).
13. Yazaki, J. et al. HaloTag-based conjugation of proteins to barcoding-oligonucleotides. *Nucleic Acids Res.* **48**, e8 (2020).
14. Liu, Y., Sawalha, A. H. & Lu, Q. COVID-19 and autoimmune diseases. *Curr. Opin. Rheumatol.* **33**, 155–162 (2021).
15. Knight, J. S. et al. The intersection of COVID-19 and autoimmunity. *J. Clin. Invest.* <https://doi.org/10.1172/JCI154886> (2021).
16. Wang, E. Y. et al. Diverse functional autoantibodies in patients with COVID-19. *Nature* **595**, 283–288 (2021).
17. Bastard, P. et al. Autoantibodies neutralizing type I IFNs are present in ~4% of uninfected individuals over 70 years old and account for ~20% of COVID-19 deaths. *Sci Immunol.* <https://doi.org/10.1126/sciimmunol.abl4340> (2021).
18. Abers, M. S. et al. Neutralizing type-I interferon autoantibodies are associated with delayed viral clearance and intensive care unit admission in patients with COVID-19. *Immunol. Cell Biol.* **99**, 917–921 (2021).
19. Mohammad, F., Green, R. & Buskirk, A. R. A systematically-revised ribosome profiling method for bacteria reveals pauses at single-codon resolution. *eLife* <https://doi.org/10.7554/eLife.42591> (2019).
20. Gu, L. et al. Multiplex single-molecule interaction profiling of DNA-barcoded proteins. *Nature* **515**, 554–557 (2014).
21. Yang, X. et al. A public genome-scale lentiviral expression library of human ORFs. *Nat. Methods* **8**, 659–661 (2011).
22. Consiglio, C. R. et al. The immunology of multisystem inflammatory syndrome in children with COVID-19. *Cell* **183**, 968–981.e967 (2020).
23. Bastard, P. et al. Autoantibodies against type I IFNs in patients with life-threatening COVID-19. *Science* <https://doi.org/10.1126/science.abd4585> (2020).
24. Zuo, Y. et al. Prothrombotic autoantibodies in serum from patients hospitalized with COVID-19. *Sci. Transl. Med.* <https://doi.org/10.1126/scitranslmed.abd3876> (2020).
25. Casciola-Rosen, L. et al. IgM anti-ACE2 autoantibodies in severe COVID-19 activate complement and perturb vascular endothelial function. *JCI Insight.* **7**, 1–18 (2022).
26. Woodruff, M. C., Ramonell, R. P., Lee, F. E. & Sanz, I. Relaxed peripheral tolerance drives *de novo* autoreactivity in severe COVID-19. *medRxiv* <https://doi.org/10.1101/2020.10.21.20216192> (2021).
27. Wang, D. et al. AAgAtlas 1.0: a human autoantigen database. *Nucleic Acids Res.* **45**, D769–D776 (2017).
28. Lloyd, T. E. et al. Cytosolic 5'-nucleotidase 1A as a target of circulating autoantibodies in autoimmune diseases. *Arthritis Care Res.* **68**, 66–71 (2016).
29. Gupta, S., Nakabo, S., Chu, J., Hasni, S. & Kaplan, M. J. Association between anti-interferon-alpha autoantibodies and COVID-19 in systemic lupus erythematosus. *medRxiv* <https://doi.org/10.1101/2020.10.29.20222000> (2020).
30. Xu, G. J. et al. Systematic autoantigen analysis identifies a distinct subtype of scleroderma with coincident cancer. *Proc. Natl Acad. Sci. USA* <https://doi.org/10.1073/pnas.1615990113> (2016).
31. Venkataraman, T. et al. Analysis of antibody binding specificities in twin and SNP-genotyped cohorts reveals that antiviral antibody epitope selection is a heritable trait. *Immunity* **55**, 174–184.e175 (2022).
32. Stoeckius, M. et al. Simultaneous epitope and transcriptome measurement in single cells. *Nat. Methods* **14**, 865–868 (2017).
33. Setliff, I. et al. High-throughput mapping of B cell receptor sequences to antigen specificity. *Cell* **179**, 1636–1646.e1615 (2019).
34. Saka, S. K. et al. Immuno-SABER enables highly multiplexed and amplified protein imaging in tissues. *Nat. Biotechnol.* **37**, 1080–1090 (2019).
35. Roman-Melendez, G. D. et al. Citrullination of a phage-displayed human peptidome library reveals the fine specificities of rheumatoid arthritis-associated autoantibodies. *EBioMedicine* **71**, 103506 (2021).
36. Roman-Melendez, G. D., Venkataraman, T., Monaco, D. R. & Larman, H. B. Protease activity profiling via programmable phage display of comprehensive proteome-scale peptide libraries. *Cell Syst.* **11**, 375–381.e374 (2020).
37. Mordstein, M. et al. Lambda interferon renders epithelial cells of the respiratory and gastrointestinal tracts resistant to viral infections. *J. Virol.* **84**, 5670–5677 (2010).
38. Ank, N. et al. Lambda interferon (IFN- λ), a type III IFN, is induced by viruses and IFNs and displays potent antiviral activity against select virus infections in vivo. *J. Virol.* **80**, 4501–4509 (2006).
39. Busnadiego, I. et al. Antiviral activity of type I, II, and III interferons counterbalances ACE2 inducibility and restricts SARS-CoV-2. *mBio* <https://doi.org/10.1128/mBio.01928-20> (2020).
40. Vanderheiden, A. et al. Type I and type III interferons restrict SARS-CoV-2 infection of human airway epithelial cultures. *J. Virol.* <https://doi.org/10.1128/JVI.00985-20> (2020).
41. Stanifer, M. L. et al. Critical role of type III interferon in controlling SARS-CoV-2 infection in human intestinal epithelial cells. *Cell Rep.* **32**, 107863 (2020).
42. Galani, I. E. et al. Untuned antiviral immunity in COVID-19 revealed by temporal type I/III interferon patterns and flu comparison. *Nat. Immunol.* **22**, 32–40 (2021).
43. Felgenhauer, U. et al. Inhibition of SARS-CoV-2 by type I and type III interferons. *J. Biol. Chem.* **295**, 13958–13964 (2020).
44. O'Brien, T. R. et al. Weak induction of interferon expression by severe acute respiratory syndrome coronavirus 2 supports clinical trials of interferon- λ to treat early coronavirus disease 2019. *Clin. Infect. Dis.* **71**, 1410–1412 (2020).
45. Andreakos, E. & Tsiodras, S. COVID-19: lambda interferon against viral load and hyperinflammation. *EMBO Mol. Med.* **12**, e12465 (2020).
46. Prokunina-Olsson, L. et al. COVID-19 and emerging viral infections: The case for interferon lambda. *J. Exp. Med.* <https://doi.org/10.1084/jem.20200653> (2020).
47. Feld, J. J. et al. Peginterferon lambda for the treatment of outpatients with COVID-19: a phase 2, placebo-controlled randomised trial. *Lancet Respir. Med.* [https://doi.org/10.1016/S2213-2600\(20\)30566-X](https://doi.org/10.1016/S2213-2600(20)30566-X) (2021).
48. Jongsma, M. A. & Litjens, R. H. Self-assembling protein arrays on DNA chips by auto-labeling fusion proteins with a single DNA address. *Proteomics* **6**, 2650–2655 (2006).
49. Gautier, A. et al. An engineered protein tag for multiprotein labeling in living cells. *Chem. Biol.* **15**, 128–136 (2008).
50. Samelson, A. J. et al. Kinetic and structural comparison of a protein's cotranslational folding and refolding pathways. *Sci. Adv.* **4**, eaas9098 (2018).
51. Tosi, L. et al. Long-adaptor single-strand oligonucleotide probes for the massively multiplexed cloning of kilobase genome regions. *Nat. Biomed. Eng.* <https://doi.org/10.1038/s41551-017-0092> (2017).
52. Mohan, D. et al. Publisher correction: PhIP-seq characterization of serum antibodies using oligonucleotide-encoded peptidomes. *Nat. Protoc.* **14**, 2596 (2019).
53. Tuckey, C., Asahara, H., Zhou, Y. & Chong, S. Protein synthesis using a reconstituted cell-free system. *Curr. Protoc. Mol. Biol.* **108**, 16.31.11–16.31.22 (2014).
54. Klein, S. L. et al. Sex, age, and hospitalization drive antibody responses in a COVID-19 convalescent plasma donor population. *J. Clin. Invest.* **130**, 6141–6150 (2020).
55. Garibaldi, B. T. et al. Patient trajectories among persons hospitalized for COVID-19. *Ann. Intern. Med.* **174**, 144 (2021).
56. Zyskind, I. et al. SARS-CoV-2 seroprevalence and symptom onset in culturally-linked Orthodox Jewish communities across multiple regions in the United States. *JAMA Open Netw.* **4**, 1–9 (2021).
57. Rose, M. R. & Group, E. I. W. 188th ENMC International Workshop: inclusion body myositis, 2–4 December 2011, Naarden, The Netherlands. *Neuromuscul. Disord.* **23**, 1044–1055 (2013).
58. Wei, Z., Zhang, W., Fang, H., Li, Y. & Wang, X. esATAC: an easy-to-use systematic pipeline for ATAC-seq data analysis. *Bioinformatics* **34**, 2664–2665 (2018).
59. Robinson, M. D., McCarthy, D. J. & Smyth, G. K. edgeR: a Bioconductor package for differential expression analysis of digital gene expression data. *Bioinformatics* **26**, 139–140 (2010).

Acknowledgements

This study was made possible by a Johns Hopkins University Provost Research Grant made through the Johns Hopkins COVID-19 Research Response Program, by a National Institute of General Medical Sciences (NIGMS) grant R01 GM127353 (to H.B.L. and B.P.), by a grant from the National Heart, Lung, and Blood Institute of the National Institutes of Health under award number K23HL151826 (to E.M.B.), by grants from the Sjögren's Syndrome Foundation and the Jerome L. Greene Foundation (to A.N.B. and H.B.L.) and by funding from the intramural research programs of the Vaccine Research

Center, National Institute of Allergy and Infectious Diseases and the National Institute of Arthritis and Musculoskeletal and Skin Diseases, National Institutes of Health. We thank S. Elledge for generously providing the human ORFeome library and the 90-aa human peptidome T7 phage display library. We thank R. Green, M. Catipovic, A. Buskirk, T. O'Donnell, P. Duggal and J. Markle for helpful discussions. We also thank J. Franklin and the Johns Hopkins Synthesis and Sequencing Core for HPLC purification of the HaloLigand conjugated RT-primer, as well as L. Orzolek and H. Hao of the Johns Hopkins Transcriptomics and Deep Sequencing Core Facility. We also thank C. Tuckey at New England Biolabs for assistance with Translation kits. The severe COVID-19 specimens used for this work were part of the Johns Hopkins Biospecimen Repository, which relies on the contribution of many patients, research teams and clinicians. We thank the members of the NIH Vaccine Research Center for pre-pandemic sample collection: B. Graham, L. Novick, J. Casazza, J. Ledgerwood, U. Sarwar, L. Chang, C. Starr Hendel, L. Holman, S. Plummer, P. Costner, I. Gorden, B. Larkin, F. Mendoza, J. Saudners, K. Zephir, M. E. Enama, G. Yamshchikov, I. Pittman and P. Williams. Parts of some figures were created with BioRender.com.

Author contributions

H.B.L. and J.J.C. conceived the project and oversaw all experiments. H.B.L., J.J.C., J.G. and P.S. wrote the manuscript. J.J.C., A.R., A.W. and H.-J.T. constructed the MIPSAs destination vector. J.J.C., J.G. and P.S. performed the MIPSAs experiments and IFN neutralization studies. J.G. and D.R.M. wrote the MIPSAs computational pipelines. J.G., X.A.Z., D.R.M., W.R.M. and Y.D. performed data analysis and edited the manuscript. B.P. and L.T. reviewed data and edited the paper. A.L.C. oversaw selection of remnant specimens from the Johns Hopkins COVID-19 Remnant Specimen Biorepository and edited the manuscript. E.M.B. and A.A.R.T. oversaw collection of COVID-19 convalescent plasma from non-hospitalized patients and edited the manuscript. A.N.B., M.R., I.Z.,

A.Z.R., J.I.S., S.J., T.L. and A.L.M. were involved in the collection and analysis of data from clinical samples and edited the manuscript.

Competing interests

H.B.L., J.J.C., J.G. and P.S. are listed as inventors on a patent application filed by Johns Hopkins University that covers the MIPSAs technology. H.B.L. is a founder of Portal Bioscience, Alchemab and ImmuneID, and an advisor to TScan Therapeutics. The other authors declare no competing interests.

Additional information

Supplementary information The online version contains supplementary material available at <https://doi.org/10.1038/s41551-022-00925-y>.

Correspondence and requests for materials should be addressed to H. Benjamin Larman.

Peer review information *Nature Biomedical Engineering* thanks the anonymous reviewer(s) for their contribution to the peer review of this work.

Reprints and permissions information is available at www.nature.com/reprints.

Publisher's note Springer Nature remains neutral with regard to jurisdictional claims in published maps and institutional affiliations.

Springer Nature or its licensor holds exclusive rights to this article under a publishing agreement with the author(s) or other rightsholder(s); author self-archiving of the accepted manuscript version of this article is solely governed by the terms of such publishing agreement and applicable law.

© The Author(s), under exclusive licence to Springer Nature Limited 2022

Reporting Summary

Nature Portfolio wishes to improve the reproducibility of the work that we publish. This form provides structure for consistency and transparency in reporting. For further information on Nature Portfolio policies, see our [Editorial Policies](#) and the [Editorial Policy Checklist](#).

Statistics

For all statistical analyses, confirm that the following items are present in the figure legend, table legend, main text, or Methods section.

n/a Confirmed

- The exact sample size (n) for each experimental group/condition, given as a discrete number and unit of measurement
- A statement on whether measurements were taken from distinct samples or whether the same sample was measured repeatedly
- The statistical test(s) used AND whether they are one- or two-sided
Only common tests should be described solely by name; describe more complex techniques in the Methods section.
- A description of all covariates tested
- A description of any assumptions or corrections, such as tests of normality and adjustment for multiple comparisons
- A full description of the statistical parameters including central tendency (e.g. means) or other basic estimates (e.g. regression coefficient) AND variation (e.g. standard deviation) or associated estimates of uncertainty (e.g. confidence intervals)
- For null hypothesis testing, the test statistic (e.g. F , t , r) with confidence intervals, effect sizes, degrees of freedom and P value noted
Give P values as exact values whenever suitable.
- For Bayesian analysis, information on the choice of priors and Markov chain Monte Carlo settings
- For hierarchical and complex designs, identification of the appropriate level for tests and full reporting of outcomes
- Estimates of effect sizes (e.g. Cohen's d , Pearson's r), indicating how they were calculated

Our web collection on [statistics for biologists](#) contains articles on many of the points above.

Software and code

Policy information about [availability of computer code](#)

Data collection All code used to generate data was implemented in R v 4.0.2. We used the MIPSAlign wrapper with the matchAlign aligner in the MIPSAlign (v.0.0.9.0) package to map all sequencing reads. Next, we used the edgeR (v.3.32.0) package with the MIPSAlign function enrichProt to determine which protein reactivities were enriched. All code is available on request. The MIPSAlign package for alignment and UCI-ORF matching is available on github (repository: jgunn123/MIPSAlign).

Data analysis MIPSAlign (v.0.0.9.0) package for alignment and UCI-ORF matching, available on github (repository: jgunn123/MIPSAlign). Heatmaps were constructed using the heatmaply (v.1.2.1) package, and all other plots were generated utilizing the ggplot2 (v.3.3.3) package. The Student's t-test was utilized to determine statistical significance for comparing distributions unless noted otherwise.

For manuscripts utilizing custom algorithms or software that are central to the research but not yet described in published literature, software must be made available to editors and reviewers. We strongly encourage code deposition in a community repository (e.g. GitHub). See the Nature Portfolio [guidelines for submitting code & software](#) for further information.

Data

Policy information about [availability of data](#)

All manuscripts must include a [data availability statement](#). This statement should provide the following information, where applicable:

- Accession codes, unique identifiers, or web links for publicly available datasets
- A description of any restrictions on data availability
- For clinical datasets or third party data, please ensure that the statement adheres to our [policy](#)

The data supporting the results in this study are available within the paper and its Supplementary Information. Source data are provided with this paper. The raw and analysed datasets are available from the corresponding author on request.

Human research participants

Policy information about [studies involving human research participants and Sex and Gender in Research](#).

Reporting on sex and gender	Because of the small samples size, subgroup analyses based on sex and gender were not performed.
Population characteristics	Population characteristics are provided in Supplementary Table 1.
Recruitment	The study cohort was defined as in patients who had: 1) a confirmed RNA diagnosis of COVID-19 from a nasopharyngeal swab sample; 2) survival to death or discharge; and 3) remnant specimens in the Johns Hopkins COVID-19 Remnant Specimen Biorepository, an opportunity sample that includes 59% of Johns Hopkins Hospital COVID-19 patients and 66% of patients with length of stay ≥ 3 days. Patient outcomes were defined by the World Health Organization (WHO) COVID-19 disease severity scale.
Ethics oversight	The study was approved by the JHU Institutional Review Board (IRB00248332, IRB00273516), with a waiver of consent because all specimens and clinical data were de-identified by the Core for Clinical Research Data Acquisition of the Johns Hopkins Institute for Clinical and Translational Research. The study team had no access to identifiable patient data.

Note that full information on the approval of the study protocol must also be provided in the manuscript.

Field-specific reporting

Please select the one below that is the best fit for your research. If you are not sure, read the appropriate sections before making your selection.

- Life sciences Behavioural & social sciences Ecological, evolutionary & environmental sciences

For a reference copy of the document with all sections, see [nature.com/documents/nr-reporting-summary-flat.pdf](https://www.nature.com/documents/nr-reporting-summary-flat.pdf)

Life sciences study design

All studies must disclose on these points even when the disclosure is negative.

Sample size	In the severe COVID-19 cohort, we analysed plasma from all severe cases that were available at the time. The remainder of wells on a 96-well plate were back-filled with an equal mix of pre-pandemic controls and mild COVID-19 convalescent plasma.
Data exclusions	One IBM sample was excluded from analysis in Fig. 4c because it was highly discordant between replicates.
Replication	To determine IFNL3 neutralizing activity, all plasma were evaluated in triplicate. Owing to limited sample availability, we have not yet replicated the IFNL3 finding in an independent cohort.
Randomization	Randomization was not relevant because the exact same testing and analytical conditions were applied to all samples.
Blinding	Blinding was not relevant because the exact same testing and analytical conditions were applied to all samples.

Reporting for specific materials, systems and methods

We require information from authors about some types of materials, experimental systems and methods used in many studies. Here, indicate whether each material, system or method listed is relevant to your study. If you are not sure if a list item applies to your research, read the appropriate section before selecting a response.

Materials & experimental systems

n/a	Involvement
<input type="checkbox"/>	<input checked="" type="checkbox"/> Antibodies
<input type="checkbox"/>	<input checked="" type="checkbox"/> Eukaryotic cell lines
<input checked="" type="checkbox"/>	<input type="checkbox"/> Palaeontology and archaeology
<input checked="" type="checkbox"/>	<input type="checkbox"/> Animals and other organisms
<input checked="" type="checkbox"/>	<input type="checkbox"/> Clinical data
<input checked="" type="checkbox"/>	<input type="checkbox"/> Dual use research of concern

Methods

n/a	Involvement
<input checked="" type="checkbox"/>	<input type="checkbox"/> ChIP-seq
<input checked="" type="checkbox"/>	<input type="checkbox"/> Flow cytometry
<input checked="" type="checkbox"/>	<input type="checkbox"/> MRI-based neuroimaging

Antibodies

Antibodies used	Anti-FLAG (Sigma), anti-HaloTag (Promega), anti-IFNa2 (InvivoGen), anti-IFNL3 (InvivoGen)
Validation	https://www.sigmaaldrich.com/catalog/product/sigma/f3165?lang=en&region=US https://www.promega.com/products/protein-detection/primary-and-secondary-antibodies/anti-halotag-monoclonal-antibody/?catNum=G9211 https://www.invivogen.com/sites/default/files/invivogen/products/files/anti_hifna_igg_tds.pdf https://www.invivogen.com/sites/default/files/invivogen/products/files/anti_hifn_lambda_vds.pdf

Eukaryotic cell lines

Policy information about [cell lines and Sex and Gender in Research](#)

Cell line source(s)	A549 cells isolated from the lung tissue of a 58-year-old Caucasian male with lung cancer.
Authentication	The cells were not authenticated.
Mycoplasma contamination	The cells were not tested for mycoplasma contamination.
Commonly misidentified lines (See ICLAC register)	No misidentified cell lines were used.